Journal of Solid State Chemistry 186 (2012) 134–141

Contents lists available at SciVerse ScienceDirect

Journal of Solid State Chemistry

journal homepage: www.elsevier.com/locate/jssc

Magnetic measurements and neutron diffraction study of the layered hybrid compounds $Mn(C_8H_4O_4)(H_2O)_2$ and $Mn_2(OH)_2(C_8H_4O_4)$

Romain Sibille [a,*], Adel Mesbah [a], Thomas Mazet [a], Bernard Malaman [a], Silvia Capelli [b], Michel François [a]

[a] Institut Jean Lamour, UMR 7198—Nancy Université, BP 70239, 54506 Vandoeuvre-lès-Nancy Cedex, France
[b] Institut Laue Langevin, 6 rue Jules Horowitz, 38042 Grenoble Cedex 9, France

ARTICLE INFO

Article history:
Received 14 September 2011
Received in revised form
1 December 2011
Accepted 5 December 2011
Available online 13 December 2011

Keywords:
Hybrid compound
Magnetic properties
Magnetic structure
Magneto-structural correlations
Low-dimensional magnet
Terephthalate

ABSTRACT

$Mn(C_8H_4O_4)(H_2O)_2$ and $Mn_2(OH)_2(C_8H_4O_4)$ layered organic–inorganic compounds based on manganese(II) and terephthalate molecules ($C_8H_4O_4^{2-}$) have been studied by DC and AC magnetic measurements and powder neutron diffraction. The dihydrated compound behaves as a 3D antiferromagnet below 6.5 K. The temperature dependence of its χT product is typical of a 2D Heisenberg system and allows determining the in-plane exchange constant $J \approx -7.4$ K through the carboxylate bridges. The magnetic structure confirms the in-plane nearest neighbor antiferromagnetic interactions and the 3D ordering. The hydroxide based compound also orders as a 3D antiferromagnet with a higher Néel temperature (38.5 K). Its magnetic structure is described from two antiferromagnetically coupled ferromagnetic sublattices, in relation with the two independent metallic sites. The isothermal magnetization data at 2 K are consistent with the antiferromagnetic ground-state of these compounds. However, in both cases, a slope change points to field-induced modification of the magnetic structure.

1. Introduction

The hybrid compounds are considered as potential multi-properties materials. They can associate, for instance, magnetic properties from the mineral component and electronic properties due to π electrons in the organic part [1–3]. Fundamental research studies have been focused on hybrid compounds as well organized systems in order to establish relationships between their structural and physical properties. During the last decade, the *M*(II)-carboxylate systems, where *M* is typically a 3*d* transition metal, have been intensely explored. A comprehensive discussion dealing with the structures and the magnetic properties of layered organic-inorganic materials – including metal-carboxylate based hybrids – can be found in [4]. The wide family of MOFs (metal-organic frameworks), interesting for applications such as catalysis and gas storage, also includes these systems [5,6]. For a rapid insight of some metal-carboxylate architectures of MOFs the reader can refer to the review articles [7,8].

1,4-benzenedicarboxylic acid (also called terephthalic acid) has led to numerous examples of new metal-organic frameworks and coordination compounds. The MOF-5 structure [9] which is a highly porous crystalline material and the MIL-53 structure [10] which exhibits reversible breathing effects upon insertion and removal of guest molecules, are famous examples. Layered compounds where metal-hydroxide layers are separated by terephthalate molecules have been intensely studied. There are two phases where diamagnetic layers are separated by terephthalate ($tp = C_8H_4O_4^{2-}$) molecules: $Zn_2(OH)_2(tp)$ [11] and $Zn_3(OH)_4(tp)$ [12]. Similar compounds made of magnetic transition metal cations have also been stabilized: $[Ni_3(OH)_2(tp)_2(H_2O)_4]\cdot 2H_2O$ [13] and $M_2(OH)_2(tp)$ with $M = Co^{2+}$ [14], Cu^{2+} [15], Fe^{2+} and Mn^{2+} [16]. Within each of these structures, the metallic layers are built upon dense metal-hydroxide networks where the metallic centers are linked by oxygen atoms leading to the existence of *M*–O–*M* magnetic exchange pathways into the layers. Another layered structure exists: $M(tp)(H_2O)_2$ where the metallic layers are made of isolated transition metal ions ($M = Mg^{2+}$, Mn^{2+}, Fe^{2+} and Cu^{2+}) [17] which are linked together by the carboxylate function of the *tp* molecule, thus leading to the existence of *M*–O–C–O–*M* magnetic exchange pathways into the 'inorganic planes'. Terephthalic acid is an interesting organic linker for magnetic metal-organic frameworks as it involves the presence of π electrons together with relatively long distances (about 10 Å) between the magnetic centers. These particular features of the *tp* molecule often lead to original magnetic behaviors as the through-space dipolar interactions compete with the through-bond exchange interactions.

The magnetic behavior of the $M_2(OH)_2(tp)$ compounds have already been studied for $M = Co^{2+}$ [14], Cu^{2+} [15] and Fe^{2+} [20]. The $Co_2(OH)_2(tp)$ magnet exhibits a giant hysteretic effect [14] and its magnetic structure has been determined [18]. $(Co_{1-x}Fe_x)_2(OH)_2(tp)$ solid solutions have also been studied in order to investigate the effect of the iron substitution on this original property. The location of the metallic elements in these solid solutions can be found in [19]. Ref. [20] describes the macroscopic magnetic properties and magnetic

* Corresponding author.
E-mail address: romain.sibille@ijl.nancy-universite.fr (R. Sibille).

0022-4596/$ - see front matter © 2011 Elsevier Inc. All rights reserved.
doi:10.1016/j.jssc.2011.12.009

structures of these solid solutions together with that of the pure iron compound. To the best of our knowledge, the magnetic properties of the $M(tp)(H_2O)_2$ compounds have not yet been studied.

In this paper, we investigate the magnetic properties of the $Mn(tp)(H_2O)_2$ and $Mn_2(OH)_2(tp)$ hybrid compounds by AC and DC magnetic measurements as well as neutron diffraction experiments. In the following, these compounds will be labeled as **1** and **2**.

The crystal structures of compounds **1** ($C2/c$) and **2** ($C2/m$) are reminded in Figs. 1 and 2, respectively. The hydrated compound **1** contains a single metallic site which consists of an isolated Mn(II) oxygen octahedron. Four equatorial oxygen atoms come from the carboxylate function of four different *tp* molecules whereas the two apical oxygen atoms pertain to water molecules. In other words, the *tp* molecules link the metallic sites together, both within and between the layers, while the water molecules separate them within the layers. The crystal structure of **2** is also layered but it contains two metallic sites (noted $M1$ and $M2$). Although they both have an octahedral coordination polyhedron, the environments of $M1$ and $M2$ are quite different. $M1$ site is at the center of an octahedron formed by four hydroxyl ions and two O-carboxylate atoms whereas $M2$'s octahedron is formed by four O-carboxylate atoms and two hydroxyl ions. The interlayer distances in **1** and **2** are 9.32 Å and 9.93 Å, respectively, and this weak difference arises mainly from the tilt angles α shown in Fig. 1 ($\approx 28^\circ$) and Fig. 2 ($\approx 24^\circ$), respectively. It is noteworthy that in **2**, the $C2/m$ space group corresponds to an average structure because the *tp* anions are located about the -1 symmetry element ($4f$ position) and are bent $\approx 24^\circ$ from the mirror plane in (010). Terephthalate molecules are therefore disordered over two equiprobable sites. However, such disorder is conditioned since, down **b**, all *tp* fragments must be coherently tilted in the same direction, while neighboring stacks (in the **a** and **c** directions) may occasionally revert the sequence [14].

2. Experimental

2.1. Synthesis

All chemicals were commercially available from *Aldrich* and used as received. Both compounds were synthesized according to the same procedure: terephthalic acid disodium salt (6 mmol, 1.2 g) was dissolved into 10 mL of distillated water. The pH of the starting solution was finely adjusted by NaOH droplets to 8.5 for the synthesis of the hydrated compound (**1**) and to 10.5 for the synthesis of the hydroxide based compound (**2**). The resulting solution was placed into a home-made 50 mL plastic reactor under

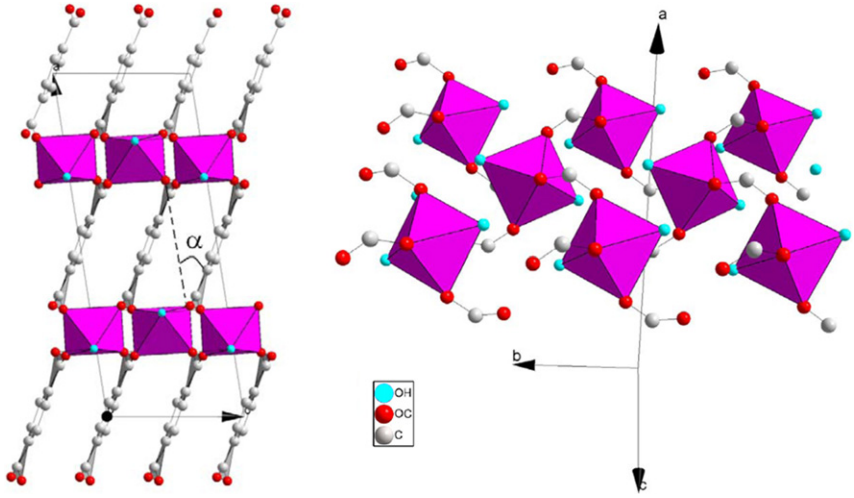

Fig. 1. Crystallographic structure of **1** viewed along the ***b*** axis (left). Structure of the metallic planes (right) showing the connection of the manganese-centered oxygen octahedra through the carboxylate functions.

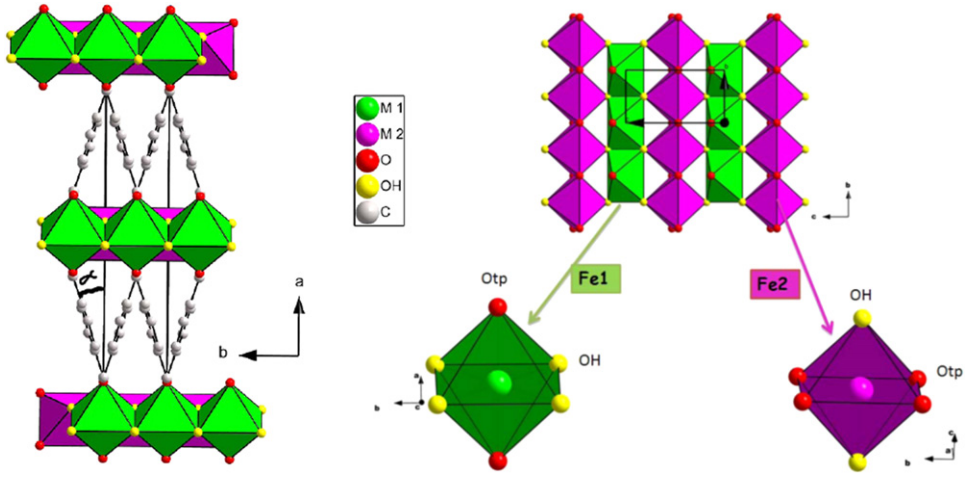

Fig. 2. Structure of $M_2(OH)_2tp$ (M=Mn, Fe, Co) viewed along the ***c*** axis (left). Structure of the metal-hydroxide layers and polyhedral representation of the environment of the $M1$ and $M2$ sites (right).

constant argon current in order to avoid the formation of manganese oxide impurities. This hermetic reactor was equipped by two injectors, a pH electrode and magnetic stirring. The system was deoxygenated during ten minutes before the simultaneous addition of the $MnCl_2 \cdot 4H_2O$ (4 mmol, 0.8 g in 10 mL water) and NaOH (0.5 M) solutions by the two injectors. The addition was driven by two peristaltic pumps (*Ismatec*) and the electrode was linked to a pH-meter (*Knick*). The two peristaltic pumps and the pH-meter were driven by a computer via the *Labworldsoft* program. The addition of the metallic salt solution was done at a constant rate while the addition rate of the basic solution was varying in order to keep a constant pH value during the whole course of the addition ($\approx$1 h). After that, the mixture was stirred for five more minutes and then sucked up by a syringe which was then transferred into a glovebox under argon atmosphere. The mixture was finally transferred into a Teflon-walled stainless steel autoclave under argon atmosphere. Following this first step, both compounds were obtained by a hydrothermal treatment at 150 °C. After three days, the autoclave was naturally cooled in air and opened under ambient atmosphere. The reaction product was collected by centrifugation, washed twice with a mixture of distilled water and ethanol (1/1) and then dried at room temperature. Such a system where the addition of reagents is finely controlled can be used as a way of increasing the crystallinity of the final product, but the main reason for using peristaltic pumps here is just to limit the formation of **1** during the synthesis of **2** by keeping a constant pH value. We note that this hydrothermal route for the synthesis of **1** was not the approach used by Kaduk [17]. Thus we have found here that **1** and **2** can be easily obtained by the same procedure depending only on the pH of the starting mixture.

2.2. Thermal analysis

Thermogravimetric (TG) measurements were performed with a 'TG/ATD 92–16.18' SETARAM instrument between 20 and 600 °C in air and using a heating rate of 1 °C/min. The thermal curves for **1** and **2** are reported in supplementary materials (Figs. S1 and S2). For compound **1** the weight loss occurs in two steps, a first one at 100–150 °C corresponding to the loss of the water molecules (−13.58% obs. −14.12% calc.) and a second step between 300 and 400 °C which is related to the degradation of the *tp* molecule (−63.67% obs. −64.33% calc.) and leading to Mn_2O_3. Compound **2** decomposes in a single stage at 320 °C (−48.61% obs. −55.64% calc.). Note that the 7% difference between observed and calculated weight losses in **2** is due to the presence of a very small amount of **1**. Final Mn_2O_3 residues were checked by Powder X-Ray Diffraction (PDF: 071-0636).

2.3. Powder X-ray diffraction (PXRD)

PXRD data were collected at room temperature using filtered Cu $K\alpha$ radiation (λ=1.5418 Å) and a reflection θ–θ geometry (Philips X-Pert Pro diffractometer). Starting from the published structures of compounds **1** and **2** [17,16], the obtained powder patterns of the two products were fitted by the Rietveld method using the Fullprof_suite software [21]. During the refinement process, soft distance constraints were applied on the terephthalate molecules: C–C=1.54(1) Å and C–O=1.36(1) Å. Final PXRD Rietveld plots for **1** and **2** are available in supplementary materials (Fig. S3) as well as the associated refinements parameters (Table S1). R_F agreement factors converge satisfactorily to values lower than 10%. Note that the small quantity of **1** in the sample of **2** was detected by PXRD and taken into account as a secondary phase during the refinements.

2.4. Magnetic measurements

DC and AC magnetic susceptibility measurements were carried out with a PPMS-9T between 2 and 300 K. The DC curves were recorded under a field of 0.5 T to determine the molar Curie constant (C_M), the paramagnetic Curie temperature (θ_p) and the effective moment (μ_{eff}). The thermal dependence of the AC susceptibility was recorded using an alternative magnetic field H_{AC}=0.5 mT and a frequency of 100 Hz without bias DC field. No correction was applied for diamagnetism. Magnetization curves were recorded at 2 K in applied fields up to 9 T.

2.5. Neutron measurements

Powder neutron diffraction experiments were carried out at the Institut Laue Langevin (ILL), Grenoble (France) using the D1b two-axis diffractometer. The D1b is a high intensity powder diffractometer with a 128° PSD (λ=2.5227 Å, step of 0.1° 2θ). Al_2O_3 was used for the refinement of the wavelength. Due to the imperfect monochromatization of the incident beam the refinements were carried out by considering a second harmonic (λ/2) contamination of 0.6% in intensity. Diffraction patterns of compounds **1** and **2** were recorded in the paramagnetic state (20 K and 50 K, respectively) and in the ordered magnetic state (1.6 K) using a standard helium cryostat. The analysis of the data was performed by Rietveld refinements using the Fullprof_suite software [21]. For both compounds, the atomic coordinates deduced from PXRD refinements were used for the neutron Rietveld refinements of the patterns recorded in the paramagnetic state. Final neutron Rietveld plots for **1** and **2** in the paramagnetic and ordered states are available in supplementary materials (Figs. S4 and S5, respectively) as well as the refinement parameters (Table S1). Owing to the very negative neutron scattering length of hydrogen atoms, the neutron data are very sensitive to the atomic coordinates of these atoms. Consequently, refinements include H atoms of *tp*, H_2O and OH groups, firstly geometrically positioned, and then fitted by imposing soft distance constraints (C–H=0.93(5) Å and O–H=0.80(5) Å). The positions of the hydrogen and non-hydrogen atoms – respectively, from neutron and X-ray refinements – are reported in Tables S2 and S3 for **1** and **2**, respectively.

In accordance with TG and PXRD experiments, the neutron diagram of **2** displays the presence of **1** ($\approx$6 wt%) as an impurity, treated as a secondary phase in the refinement process.

At 1.6 K, in each case, refinements of the magnetic structure were, in a first step, performed on a "difference pattern" between the paramagnetic state and ordered state patterns. The refinements were performed in the "spherical coordinates procedure" of the Fullprof software. The three extra parameters characterizing the atomic magnetic moments correspond to the value of μ_{Mn} (in Bohr magnetons), the spherical Phi angle with *x* axis and the spherical Theta angle with *z* axis (Table 1). Since this mode works only if the *z* axis is perpendicular to the (*x*,*y*) plane, the present monoclinic space groups (*C*2/*m* and *C*2/*c*) were described in the Laue Class 1 1 2/*m* during the refinements. In a second step, in order to refine the others parameters, a final refinement has been performed on the neutron patterns recorded at 1.6 K.

3. Results and discussion

3.1. Magnetic measurements

Note that all the magnetic values are given per mol of Mn(II), i.e. per mol or per half mol of compounds **1** and **2**, respectively.

Table 1
Crystallographic data and neutron Rietveld refinement parameters.

	$Mn(H_2O)_2tp$		$Mn_2(OH)_2tp$	
	20 K	**1.6 K**	**50 K**	**1.6 K**
Space group	*C*2/*c* (nuclear)	*P*2/*m* (magnetic)	*C*2/*m* (nuclear)	*P*2/*m* (magnetic)
a **(Å)**	18.561(3)	18.561(3)	19.934(3)	19.932(3)
b **(Å)**	6.557(1)	6.556(1)	3.394(1)	3.393(1)
c **(Å)**	7.367(1)	7.367(1)	6.507(1)	6.505(1)
β **(deg.)**	98.0(1)	98.0(1)	95.2(1)	95.2(2)
f_{cor}	1.00	1.00	1.03	1.04
Theta (deg.)	–	90[a]	–	0[b]
Phi (deg.)	–	40(4)[a]	–	0[b]
μ_{Mn} (μ_B)	–	4.6(1)	–	Mn1: 4.6(1) Mn2: 4.3(1)
R_{magn} (%)	–	7	–	6
χ^2	–	11	–	16

[a] The Mn magnetic moment is in the (010) plane and its direction makes an angle of about 40° with the ***a*** axis in the *C*2/*c* space group description.
[b] The moments are aligned along the two-fold axis i.e. along the ***b*** axis in the *C*2/*m* space group description (see text).

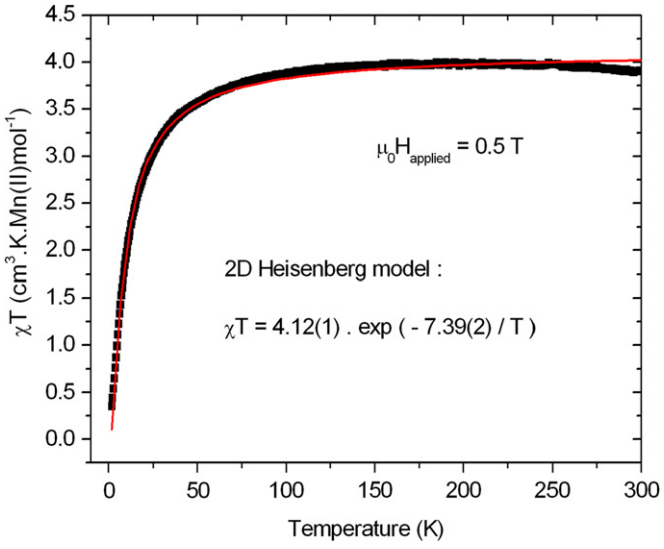

Fig. 3. Thermal variation of the χT product of **1**. The red curve represents the best fit to the exponential function. (For interpretation of the references to color in this figure legend, the reader is referred to the web version of this article.)

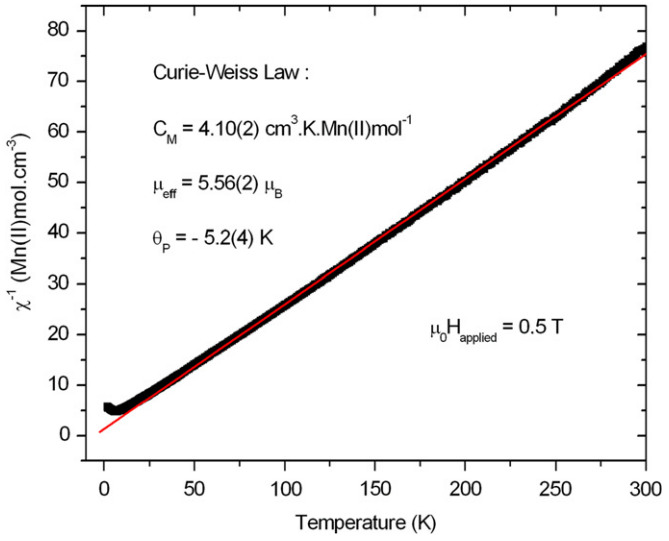

Fig. 4. Reciprocal DC susceptibility as a function of temperature for **1**. The red line is the best fit to the Curie–Weiss law in the 300–50 K range. (For interpretation of the references to color in this figure legend, the reader is referred to the web version of this article.)

3.1.1. $Mn(tp)(H_2O)_2$

The value of the χT product (Fig. 3) at 300 K (3.95 $cm^3\ K\ mol^{-1}$) is not so far from the spin-only value attempted for high-spin Mn^{2+} ions (4.38 $cm^3\ K\ mol^{-1}$). It remains almost constant from 300 K to around 70 K and then strongly decreases to 0.35 $cm^3\ K\ mol^{-1}$ at 2 K. This behavior is typical of the presence of antiferromagnetic (AF) interactions. Fitting χ^{-1} vs. T to the Curie–Weiss law in the 300–50 K range (Fig. 4) allows to determine a small negative paramagnetic temperature $\theta_P = -5.2(4)$ K. This fit yields an effective moment of 5.56(2) μ_B (C_M=4.10(2) $cm^3\ K\ mol^{-1}$), close to the theoretical value of an S=5/2 free ion (5.92 μ_B). The plot of χ_{DC} vs. T (Fig. 5) clearly shows that an AF order takes place at T_N=6.5(1) K. The AF character of the magnetic order is corroborated by AC magnetic measurements (inset of Fig. 5) that show the occurrence of a sharp peak in the in-phase component at 6.5 K, without any corresponding signal in the out-of-phase component. As shown in Fig. 3, the variation of the χT product in the 300–2 K temperature range is well fitted by the exponential function $\chi T = C \times \exp(E/kT)$. The best fit values are C=4.12(1) $cm^3\ K\ mol^{-1}$, the Curie constant and $E/k = -7.39(2)$ K the overall exchange coupling energy which points out the weakness of the AF interactions in this compound. Such a small exchange constant agrees with the low T_N of **1**. The

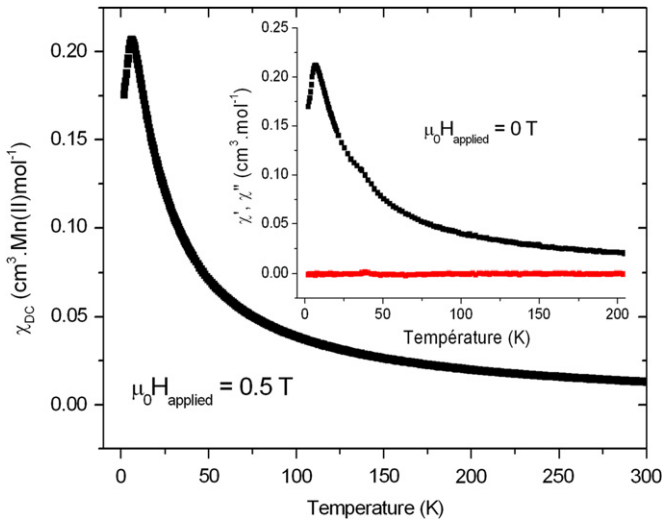

Fig. 5. Thermal dependence of the χ_{DC} and χ_{AC} (inset) susceptibilities for **1**.

exponential variation of the χT product is characteristic of a 2D Heisenberg system [22–24]. The utilized model takes into account one single exchange energy and is thus well suited for compound **1** where all the metal atoms are linked together by the same *M*–O–C–O–*M* pathways. These superexchange pathways are known as being poor magnetic media, in agreement with the small exchange constant deduced above.

The magnetization curve of **1** at 2 K is presented in Fig. 6. For low fields, the linear variation without any field hysteresis is characteristic of the AF ground-state. A not obvious but noticeable slope change is recorded at a threshold field $\mu_0 H_c = 1.22$ T and evidenced by the presence of a peak in the $dM_{DC}/d\mu_0 H$ vs. $\mu_0 H$ curve. This suggests a field-induced modification of the magnetic structure that might correspond to a canted arrangement. Above the threshold field $\mu_0 H_c$, M_{DC} increases almost linearly without field hysteresis up to $\mu_0 H = 9$ T. The magnetization value obtained in the maximum field of 9 T is 3.35 $\mu_B \cdot$ Mn(II)mol^{-1}. This value is close to that expected for a full alignment of the Mn moments, indicating that the AF magnetic structure is very sensitive to the applied field. This behavior is related to the low value of the in-plane exchange constant.

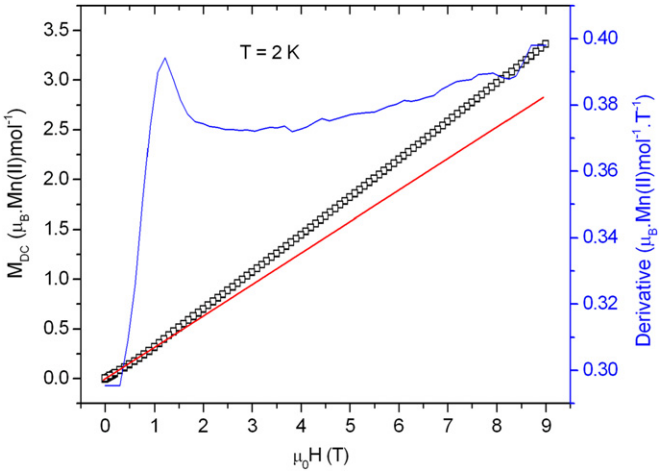

Fig. 6. Field dependence of the magnetization of **1** at 2 K and its derivative. The red line is a guide evidencing the change of slope. (For interpretation of the references to color in this figure legend, the reader is referred to the web version of this article.)

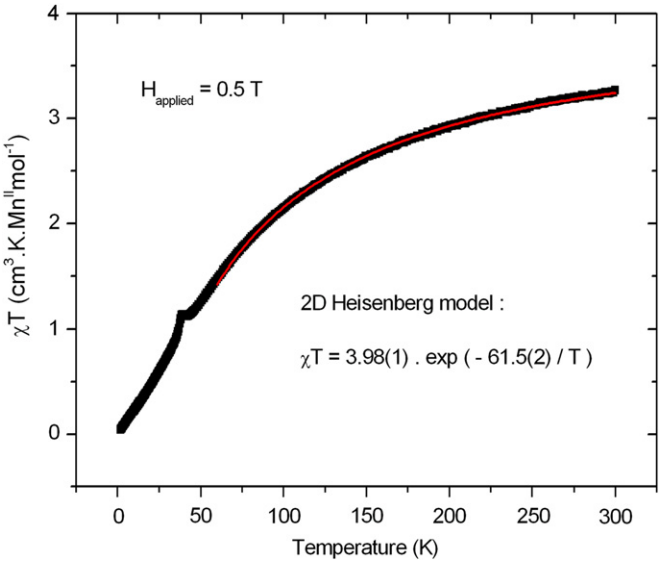

Fig. 7. Thermal variation of the χT product of **2**. The red curve represents the best fit to the exponential function. (For interpretation of the references to color in this figure legend, the reader is referred to the web version of this article.)

3.1.2. $Mn_2(OH)_2(tp)$

In the case of compound **2**, the χT product (Fig. 7) decreases continuously from 300 K (3.24 cm^3 K mol^{-1}) to 2 K (0.35 cm^3 K mol^{-1}) with a peak of very low magnitude at 38.5 K. This behavior is again characteristic of the presence of antiferromagnetic (AF) interactions. The room temperature value of χT should be carefully considered as it may be underestimated because of the presence of compound **1** in the sample. The fit of χ^{-1} vs. T to the Curie–Weiss law in the 300–100 K range (Fig. 8) affords values consistent with this first observation: a large negative paramagnetic temperature $\theta_P = -99.5(4)$ K and an effective magnetic moment of 5.93(2) μ_B ($C_M = 4.4(2)$ cm^3 K mol^{-1}), very close to that expected value for an $S = 5/2$ ion. The temperature dependence of both the χ_{DC} and the real part of χ_{AC} shows a sharp peak at 38.5(1) K (Fig. 9). The lack of anomaly in the imaginary part of χ_{AC} clearly indicates that an AF structure is stabilized below this temperature. The temperature

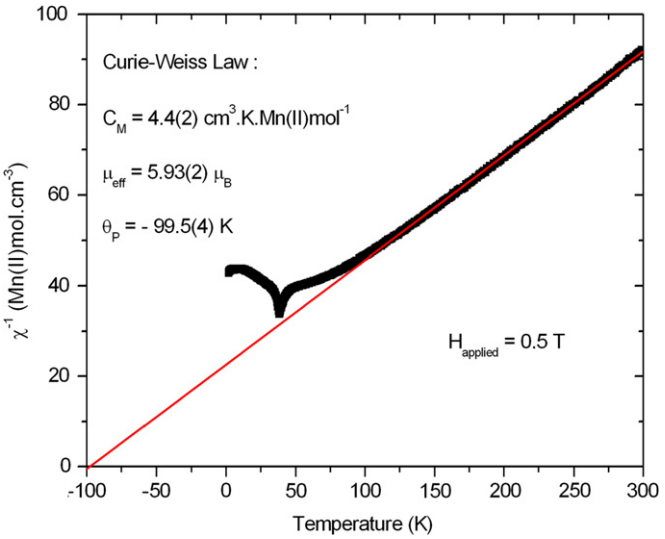

Fig. 8. Inverse of the DC susceptibility as a function of temperature for **2**. The red line is the best fit to the Curie–Weiss law in the range 300–100 K. (For interpretation of the references to color in this figure legend, the reader is referred to the web version of this article.)

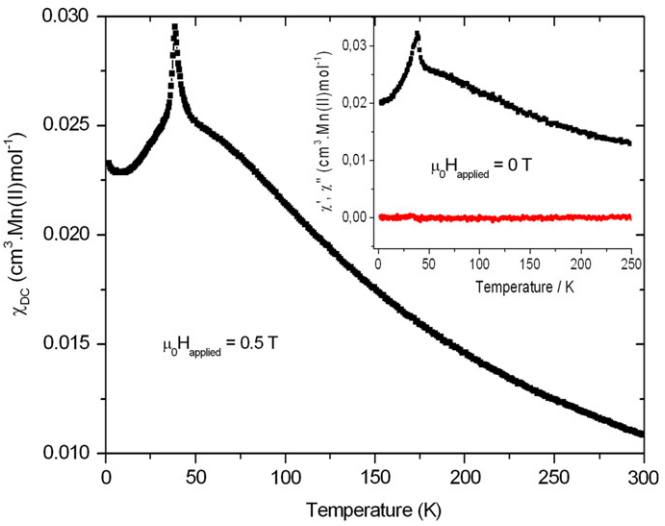

Fig. 9. Thermal dependence of the χ_{DC} and χ_{AC} (inset) susceptibilities for **2**.

dependence of the χT product for $T > T_N$ can be fitted with the 2D Heisenberg model previously used for **1**. The fit yields a Curie constant of 3.98(1) $cm^3\,K\,mol^{-1}$ and an overall in-plane exchange coupling E/k of $-61.5(2)$ K. Compared to the small exchange constant found for **1**, this larger value agrees with the higher T_N determined for **2.** The use of the 2D Heisenberg model in the case of **2** is however less justified than for **1**, because of the complex inorganic layers that include two different magnetic sites and multiple exchange pathways. Further, such a quantitative analysis of the magnetic data of **2** should be carefully considered because of the presence of **1** (see 'Experimental Section').

The magnetization curve of **2** at 2 K is presented in Fig. 10. Its variation remains almost linear without field hysteresis for applied fields below $\mu_0 H_c = 5.65$ T. Above this threshold field, a slope change is observed and evidenced by the peak in the $dM_{DC}/d\mu_0 H$ vs. $\mu_0 H$ curve. Again, this behavior likely indicates a field-induced modification of the magnetic structure. The magnetization recorded in a magnetic field of 9 T is 0.42 $\mu_B \cdot$ Mn(II)mol^{-1}.

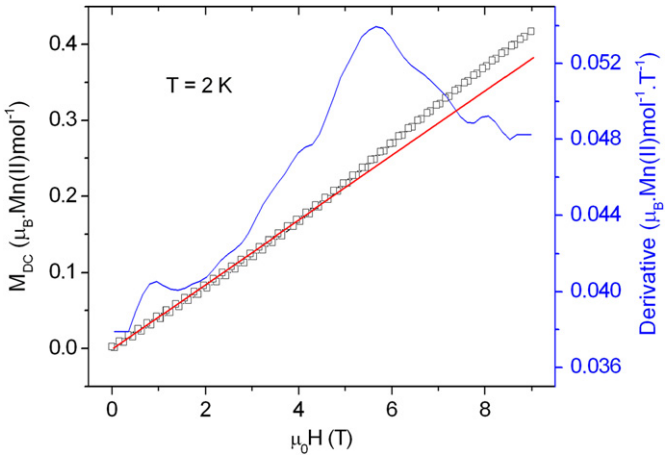

Fig. 10. Field dependence of the magnetization of **2** at 2 K and its derivative. The red line is a guide evidencing the change of slope. (For interpretation of the references to color in this figure legend, the reader is referred to the web version of this article.)

Compared to the large value found for **1**, this lower magnetization value agrees with the stronger in-plane coupling determined for the antiferromagnet **2**.

3.2. Neutron diffraction study

Crystallographic data and neutron Rietveld parameters for **1** (20 K and 1.6 K) and **2** (50 K and 1.6 K) are summarized in Table 1. It is worth noting that **1** is characterized by only one Mn site whereas **2** is characterized by two independent Mn sublattices.

3.2.1. $Mn(tp)(H_2O)_2$

Fig. 11 shows the neutron diffraction patterns recorded at 20 K and 1.6 K as well as the resulting "difference pattern". Ten magnetic lines are easily indexed in a magnetic unit cell having the metric of the chemical unit cell. The lack of (hkl) reflections with $h+k=2n+1$ implies that the magnetic structure is characterized by a C translation mode. Moreover, the growth of the (h01) reflections with $l=2n+1$ indicates that the magnetic moment arrangement does not respect the c glide of the chemical unit cell. These results imply that the Mn moments are antiferromagnetically coupled along the [001] direction while they are ferromagnetically coupled in the (a,b) plane (Fig. 12). The best refinements show that the Mn magnetic moments lie in the (010) plane and that their orientation makes an angle of about 40° with the ***a*** axis (55° *with the* ***c*** *axis*). From a local point of view, the moments are ≈18° tilted from the equatorial plane of the oxygen octahedron. The refinements lead to a value of 4.6(1) μ_B for the Mn(II) magnetic moment. In agreement with the observed macroscopic magnetic behavior described in the previous section as well as with the moment value expected for a high-spin Mn^{2+} ion in octahedral oxygen environment.

3.2.2. $Mn_2(OH)_2(tp)$

Fig. 13 shows the neutron diffraction patterns recorded at 50 K and 1.6 K for **2** as well as and the resulting "difference pattern". The ten magnetic reflections observed on the "difference pattern" are characteristic of an antiferromagnetic ordering of the two Mn sublattices. The magnetic peaks are easily indexed in the chemical cell according to (−101), (101), (−301), (301), (−501), (501),

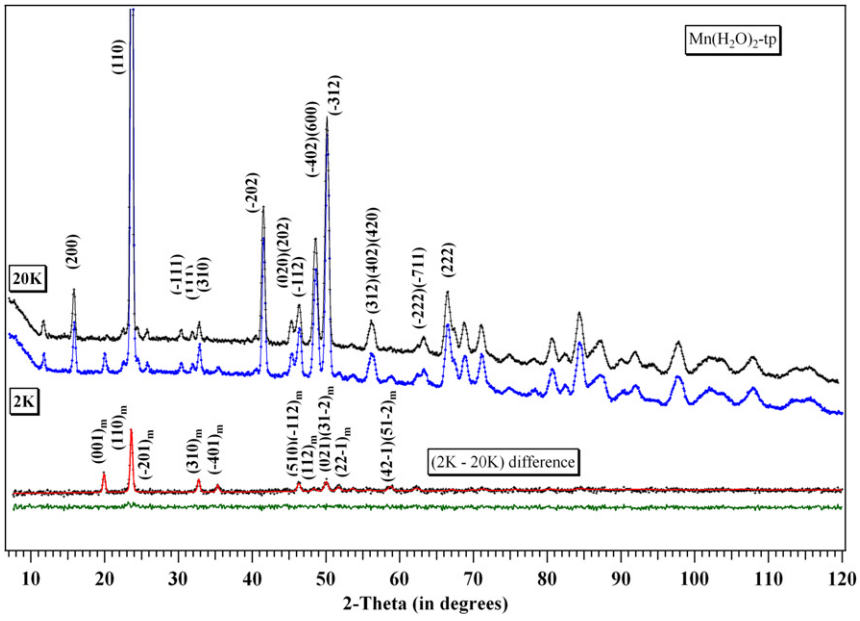

Fig. 11. Observed neutron diffraction patterns of **1** at 20 K and 1.6 K and observed and calculated neutron diffraction resulting "difference pattern".

(410), (−410), (−701) and (701). All of these reflections obey the limiting reflection condition (hkl) with $h+k=2n+1$. This implies that the magnetic structure is characterized by an anti-C translation mode, namely both Mn_1 and Mn_2 sublattices are antiferromagnetic. The lack of $0k0$ reflections indicates that the moments are aligned along the ***b*** axis. Moreover, the lack of the $h00$ reflections suggests that the Mn^{2+} moments on Mn1 and Mn2 have very close amplitudes. The best refinements lead to the magnetic structure sketched in Fig. 14. The moments on both the Mn1 and Mn2 sublattices are parallel to the ***b*** axis with an amplitude of about 4.5(1) μ_B, in agreement with the expected value for Mn^{2+} ions with $S=5/2$ (Table 1). The magnetic structure of $Mn_2(OH)_2tp$ is built upon ferromagnetic chains of [Mn_1O_6] and [Mn_2O_6] octahedra running along [010], antiferromagnetically coupled in each (100) plane.

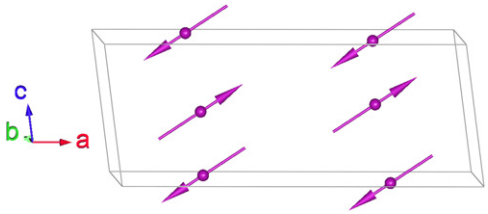

Fig. 12. Magnetic structure of **1**.

The easy magnetization axes of the Mn1 and Mn2 sublattices are thus directed along the median of the equatorial plane of the respective $Mn1O_6$ and $Mn2O_6$ octahedra. These couplings are in agreement with the Goodenough rules [25,26]. For example, as it can be seen in Fig. 14, the angles "Mn1–OH–Mn1" and "Mn2–O_{tp}–Mn2" are 99° and 103°, respectively, implying a weak ferromagnetic coupling along the [010] direction. By contrast, the angle "Mn1–OH–Mn2" is 117° which is a coherent value with a weak AF coupling between the two types of manganese chains.

3.3. Comparison with $M_2(OH)_2(tp)$ compounds

Since the magnetic properties of $M_2(OH)_2(tp)$ compounds have been largely studied for M=Co [14], Fe [16] and Cu [15], it is also interesting to compare them with those of $Mn_2(OH)_2(tp)$. The magnetic structure of **2** is isotypic with that of $Fe_2(OH)_2(tp)$ [20].

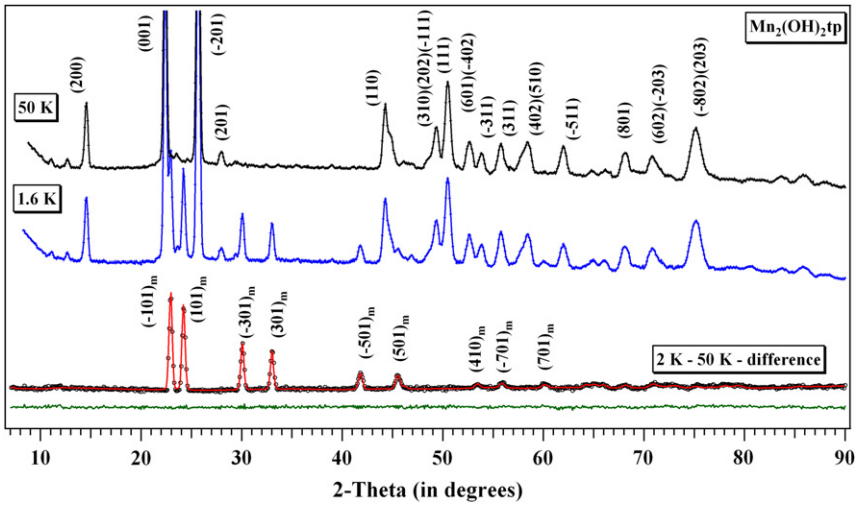

Fig. 13. Observed neutron diffraction patterns of **2** at 50 K and 1.6 K and observed and calculated neutron diffraction resulting "difference pattern".

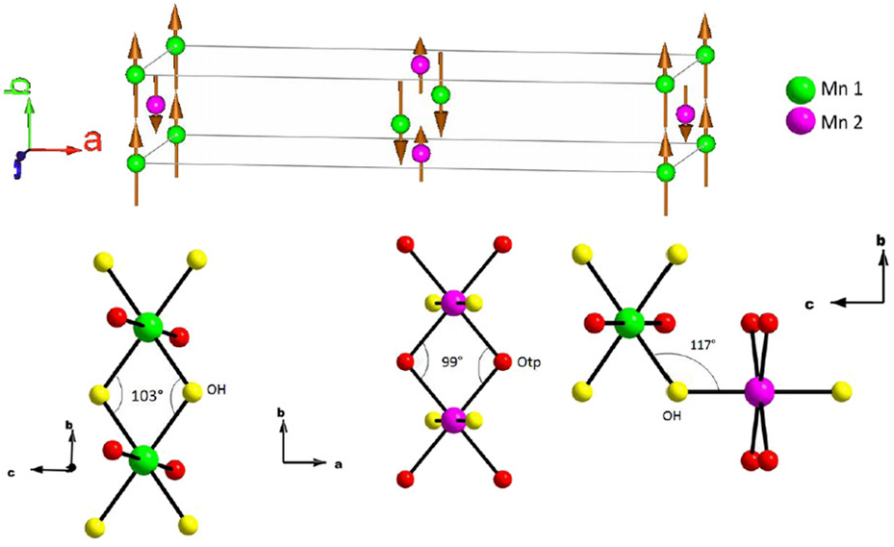

Fig. 14. Magnetic structure of **2** (top) and local structure in **2** showing the geometry of the magnetic exchange pathways Mn1–Mn1, Mn1–Mn2 and Mn2–Mn2 (bottom).

It is interesting to remind here that the cobaltous analog also displays a similar magnetic structure but with the moments aligned along the ***c*** axis [18] and that the (100) cobalt(II) planes are uncompensated due to different values of the ordered moments on each inequivalent metallic site. Moreover, its 3D magnetic structure (T_N=48 K) is basically antiferromagnetic between the layers but collinear or noncollinear spin arrangements are stabilized due to the thermal variation of the anisotropy field, including a magnetic field induced canted phase [14]. The iron based compound is also basically antiferromagnetic (T_N=66 K) between the layers but without the presence of any field induced canted phase. The copper compound exhibits drastically different properties, in-plane ferromagnetic interactions (explained by the Jahn–Teller elongation known for Cu^{2+}) are present and lead to the stabilization of a 3D ferromagnetic order (T_C=4.5 K).

Consequently, the macroscopic behavior of $Mn_2(OH)_2(tp)$ is strongly related to that of the iron analog. Both compounds exhibit the same magnetic structure and very close macroscopic magnetic properties. The difference between their Néel temperatures could be understood by taking into account different effects as (i) the larger ionic radius of Mn^{2+} high-spin compared to Fe^{2+} high-spin, thus making through-bond exchange pathways longer for the manganese compound, or (ii) the occurrence of an orbital contribution for the iron compound.

4. Conclusion

We have studied the macroscopic magnetic properties and magnetic structures of two layered hybrid compounds involving Mn^{2+} ions and terephthalate molecules. The hydrated compound $Mn(tp)(H_2O)_2$ is an antiferromagnet with a low magnetic ordering temperature (T_N=6.5 K). This result is not surprising since the in-plane magnetic pathways through the carboxylate functions as well as the interactions via the terephthalate molecules are known to be poor magnetic media generally leading to antiferromagnetic coupling. The hydroxide based compound $Mn_2(OH)_2(tp)$ is also an antiferromagnet but with a significantly larger magnetic ordering temperature (T_N=38.5 K). This difference can be understood by taken into account the different topologies of the spin layers. In the latter compound, the magnetic centers are more condensed and their polyhedrons are edge-sharing thus leading to more efficient magnetic pathways. In both cases, the low-temperature isothermal field dependence of magnetization shows a slope change which likely corresponds to a modification of the magnetic structure. The threshold field is of moderate magnitude (1.22 T) for the hydrated compound, while it is significantly higher (5.65 T) for the hydroxide based compound. Again, this observation agrees with the differences found in the strength of the in-plane exchange interactions and in ordering temperatures. Conclusively, this work has allowed studying the influence of the layer's topology on the magnetic properties of layered hybrid compounds while keeping some other parameters constant (identical interlayer linker, very close interlayer distances and identical magnetic element).

Acknowledgments

We are indebted to the Institut Laue Langevin (Grenoble, France) for the provision of research facilities. The authors are grateful to Lionel Aranda (Institut Jean Lamour, Nancy Université) for thermogravimetric measurements.

Appendix A. Supporting information

Supplementary data associated with this article can be found in the online version at doi:10.1016/j.jssc.2011.12.009.

References

[1] R. Clément, P.G. Lacroix, D. O'Hare, J. Evans, Adv. Mater. 6 (1994) 794.
[2] E. Coronado, J.R. Galan-Mascaros, C.J. Gomez-Garcia, V. Laukhin, Nature 408 (2000) 447.
[3] P.G. Lacroix, I. Malfant, Chem. Mater. 13 (2) (2001) 441.
[4] P. Rabu, M. Drillon, Adv. Eng. Mater. 5 (2003) 189.
[5] G. Férey, Chem. Mater. 13 (2001) 3084.
[6] J.L.C. Rowsell, O.M. Yaghi, Micropor. Mesopor. Mater. 73 (2004) 3.
[7] C.N.R. Rao, S. Natarajan, R. Vaidhyanathan, Angew. Chem., Int. Ed. 43 (2004) 1466.
[8] N. Guillou, C. Livage, G. Férey, Eur. J. Inorg. Chem. (2006) 4963.
[9] Hailian Li, Mohamed Eddaoudi, M. O'Keeffe, O.M. Yaghi, Nature 402 (1999) 276.
[10] C. Serre, F. Millange, C. Thouvenot, M. Noguès, G. Marsolier, D. Louër, G. Férey, J. Am. Chem. Soc. 124 (2002) 13519.
[11] A. Carton, A. Mesbah, L. Aranda, P. Rabu, M. François, Sol. State Sci. 11 (2009) 818.
[12] A. Carton, S. Abdelouhab, G. Renaudin, P. Rabu, M. François, Sol. State Sci. 8 (2006) 956.
[13] A. Carton, A. Mesbah, T. Mazet, F. Porcher, M. François, Sol. State Sci. 9 (2007) 465.
[14] Z.L. Huang, M. Drillon, N. Masciocchi, A. Sironi, J.T. Zhao, P. Rabu, P. Panissod, Chem. Mater. 12 (2000) 2805.
[15] S. Abdelouhab, M. François, E. Elkaim, P. Rabu, Sol. State Sci. 7 (2005) 227.
[16] A. Carton, A. Mesbah, M. François, P. Rabu, Z. Kristallogr. (Suppl. 26) (2007) 581.
[17] J.A. Kaduk, Acta Cryst. B58 (2002) 815.
[18] R. Feyerherm, A. Loose, P. Rabu, M. Drillon, Sol. State Sci. 5 (2003) 321.
[19] A. Mesbah, B. Malaman, T. Mazet, R. Sibille, M. François, CrystEngComm. 12 (2010) 3126.
[20] A. Mesbah, R. Sibille, T. Mazet, B. Malaman, S. Lebègue, M. François, J. Mater. Chem. 20 (2010) 9386.
[21] J. Rodriguez-Carvajal, M.T. Fernandez-Diaz, J.L. Martinez, J. Phys.: Condens. Matter 3 (1991) 3215.
[22] F. Suzuki, N. Shibata, C. Ishii, J. Phys. Soc. Jpn. 63 (1994) 1539.
[23] J. Souletie, P. Rabu, M. Drillon, in: J.S. Miller, M. Drillon (Eds.), Magnetism: Molecules to materials, vol. V, WILEY-VCH Verlag GmbH Co. KGaA, Weinheim, 2005, pp. 347–377.
[24] E.M. Bauer, C. Bellitto, G. Righini, M. Colapietro, G. Portalone, M. Drillon, P. Rabu, Inorg. Chem. 47 (2008) 10945.
[25] J.B. Goodenough, Magnetism and Chemical Bond, John Wiley and Sons Publ, New York, 1963.
[26] R.L. Carlin, Magnetochemistry, Springer-Verlag, Berlin, 1986.